

## RESEARCH ARTICLE

# Robocasting of ordered mesoporous silica-based monoliths: Rheological, textural, and mechanical characterization

Emiliano S. Dal Molin<sup>1</sup>  | Laura M. Henning<sup>1</sup> | Julian T. Müller<sup>1</sup>  |  
 Glen J. Smales<sup>2</sup>  | Brian R. Pauw<sup>2</sup> | Maged F. Bekheet<sup>1</sup>  | Aleksander Gurlo<sup>1</sup>  |  
 Ulla Simon<sup>1</sup> 

<sup>1</sup>Technische Universität Berlin, Faculty III Process Sciences, Institute of Material Science and Technology, Chair of Advanced Ceramic Materials, Berlin, Germany

<sup>2</sup>Bundesanstalt für Materialforschung und -prüfung (BAM), Division 6.5 – Polymers in Life Sciences and Nanotechnology, Berlin, Germany

## Correspondence

Emiliano S. Dal Molin, Technische Universität Berlin, Faculty III Process Sciences, Institute of Material Science and Technology, Chair of Advanced Ceramic Materials, Straße des 17. Juni 135, 10623, Berlin, Germany.

Email:

[Emiliano.dalmolin@ceramics.tu-berlin.de](mailto:Emiliano.dalmolin@ceramics.tu-berlin.de)

## Funding information

Einstein Foundation Berlin; UniSysCat

## Abstract

Hierarchically porous, high-surface-area silica materials are excellent candidates for multiple applications like catalysis and environmental remediation. Shaping these materials with additive manufacturing (AM) techniques, like robocasting, could enable their use with the benefit of on-demand, customized shaping and maximizing performance. Herein, ordered mesoporous silica COK-12 slurries were robocasted into monoliths, containing different ratios of uncalcined COK-12 and sodium bentonite (0–25 wt.%). The rheology of the mixed slurries is characterized by lower flow indexes (0.69 vs. 0.32) and higher yield stresses (96 vs. 259 Pa) compared to pure COK-12 ones. Monoliths were printed in woodpile structures and calcined at 600°C. Micro-CT measurements showed a linear shrinkage of 25% after calcination. Mechanical characterization showed increased uniaxial strength ( $0.20 \pm 0.07$  to  $1.0 \pm 0.3$  MPa) with increasing binder/solids ratio from 13 to 25%. The amorphous, mesoporous structure of COK-12 was retained. The structures exhibited open porosities of  $52 \pm 4\%$  and showed higher specific mesopore volumes, and increased average mesopore size (6 vs. 8 nm) compared to COK-12. Small-angle x-ray scattering analysis revealed an increased lattice parameter (10.3 vs. 11.0 nm) and reduced wall thickness (3.1 nm vs. 4.1 nm) of the COK-12 in the monoliths. These properties indicate suitability for their application as porous supports and adsorbents.

## KEYWORDS

additive manufacturing, OMS, porous materials, robocasting

## 1 | INTRODUCTION

Robocasting, or Direct Ink Writing, is a material extrusion additive manufacturing (AM) method<sup>[1–7]</sup> that enables the shaping of functional materials into specific/optimized 3D

forms,<sup>[8–13]</sup> which can then be used in place of simple powders, pelletized materials or traditional straight-channeled monoliths. This can mitigate health risks associated with handling ultrafine particles<sup>[14]</sup> and increase performance by using optimized structures with a greater

This is an open access article under the terms of the [Creative Commons Attribution](https://creativecommons.org/licenses/by/4.0/) License, which permits use, distribution and reproduction in any medium, provided the original work is properly cited.

© 2023 The Authors. *Nano Select* published by Wiley-VCH GmbH.

surface-to-volume ratio.<sup>[15]</sup> To date, several applications have implemented 3D-printed functional materials.<sup>[10,16–23]</sup> In applications mainly driven by surface processes such as gas adsorption or catalysis, materials capable of exhibiting high pore volume and surface areas while maintaining adequate mechanical and chemical properties are required to ensure long-lasting service and avoid accidental breakage or disaggregation.<sup>[24]</sup> A typical robocasting process begins with the design of a geometry using computer assisted design (CAD). The designed geometry is then converted using slicing software into a set of computer-readable instructions, which are then fed into a 3D printer capable of extruding a slurry of suitable rheology to retain the chosen shape. This rheology requirement is usually met by adding clays, polymers, or a combination of both.<sup>[1]</sup> A suitable solvent and a dispersant are the final common ingredients that serve to disperse the rest of the materials into one homogeneous mixture. The lack of an adequate statement of the rheological properties of robocasted slurries is a recognized problem.<sup>[1,25–27]</sup>

Robocasting allows for great flexibility in the composition of the slurry used, allowing for the facile integration of materials with useful functionalities into the print, as long as the processing does not affect them. This makes robocasting an ideal technique for printing structures with low pressure drop (which reduces pumping costs, and is especially desirable in any continuous flow process), even for nanomaterials with high surface area, such as mesoporous metal oxides.<sup>[20,22,28]</sup> One heavily researched class of materials for catalysis and gas adsorption is ordered mesoporous silica (OMS).<sup>[29,30]</sup> OMSs are silica-based materials with very high specific surface area (SSA), pore volume, and well-defined ordered mesopore (i.e., with pores ranging in size from 2 to 50 nm that are arranged periodically with the silica matrix). These characteristics of OMSs depend on their synthetic routes. OMSs have found their place as one of the most versatile types of materials.<sup>[31,32]</sup> Their textural properties and surface functionalization can be altered in various ways, allowing their use for a wide range of purposes.<sup>[33]</sup> However, these advanced materials are commonly obtained as fine powders from synthesis, causing high-pressure drops when used in chemical reactors or in filtration devices, operational concerns due to the risk of inhalation, and a complicated segregation process due to their size. Additionally, the most used OMS, such as SBA-15, SBA-16, MCM-41, and KIT-6, usually utilize the expensive tetraethoxysilane (TEOS) as a silica source in their respective syntheses as well as highly concentrated acids or bases.<sup>[34–36]</sup> A less commonly used type of OMS, COK-12, invented by Jammaer et al.,<sup>[37,38]</sup> is synthesized using an environmentally friendlier synthesis route than others. In particular, the TEOS precursor used in synthe-

sizing most OMS can be replaced with the much safer and economical sodium silicate in the case of COK-12. Furthermore, COK-12 requires only citric acid and its sodium salt as pH regulators, and while it still requires the use of a petroleum-derived soft-template, the entire synthesis can be carried out in water at room temperature (RT) and ambient pressure. Our group has previously reported on the modification,<sup>[39–42]</sup> upscaling,<sup>[38,43]</sup> and shaping<sup>[44]</sup> as well as the application<sup>[45,46]</sup> of COK-12. Additionally, a number of other groups have utilized COK-12 for different purposes.<sup>[47–52]</sup>

COK-12 is an excellent candidate for incorporation into a functional AM monolith. Previous work has studied the influence of sintering methods, and found that compaction followed by conventional sintering preserves some mesoporosity and that spark plasma sintering achieved higher mechanical strength.<sup>[44]</sup> These methods are, however, not easily applicable to a monolith with a complex structure. To avoid high sintering temperatures and thus loss of mesoporosity<sup>[42,44,39]</sup> a low-cost, widely used, and sustainable inorganic binder, sodium bentonite (NaBent), is used to lower the processing temperature and diminish the loss of these useful properties of similar OMS (i.e., SBA-15) in AM. This binder was also explored in additively manufactured aminosilica monoliths in the context of gas adsorption and surface modification.<sup>[16]</sup>

This work aims to provide a detailed procedure for the AM of COK-12 monoliths. For that purpose, we explored different weight ratios of uncalcined COK-12 using NaBent as an inorganic binder. Using uncalcined COK-12 and incorporating a binder allows for the use of lower calcination temperatures and lowers the amount of time COK-12 is exposed to high temperatures, which protects the COK-12's desired high surface area and pore volume. The rheology of the obtained slurries was thoroughly investigated and compared to the rheology of other reported printable slurries and some proposed printability measurements. The printed monoliths were extensively characterized to measure the effects of slurry composition on their different properties. The porous network was characterized by nitrogen sorption and small-angle x-ray scattering (SAXS), and the influence of the manufacturing process on the pore network was measured. The effect of the thermal treatment on phase composition and weight loss was provided by x-ray diffraction (XRD) and thermogravimetric analysis coupled with mass spectroscopy (TGA-MS). Finally, the mechanical and geometric properties of the monoliths were measured by uniaxial compression tests and micro-computer tomography (micro-CT). The results of this work pave the way for the rational formulation of future porous-metal-oxide-based slurries and their widespread use and fabrication.

**TABLE 1** Detailed composition of slurries used to robocast the monoliths employed in this work.

Sample	Solids			Water (wt.%)	Liquids	
	NaBent to solids ratio <sup>a</sup> (%)	Uncalcined COK-12 (wt.%)	NaBent (wt.%)		MF-50 <sup>b</sup> (wt.%)	Dispersant (wt.%)
NB-COK-25-P	25.0	27.0	9.0	63.1	0.9	0.30
NB-COK-18-P	18.2	30.7	6.8	61.4	1.0	0.34
NB-COK-13-P	13.5	33.7	5.2	59.9	1.1	0.38

<sup>a</sup>NaBent to solids ratio is defined as NaBent (wt.)/(NaBent (wt.) + uncalcined COK-12 (wt.)).

<sup>b</sup>MF-50 is considered a liquid as it dissolves in the water present in the mixture.

## 2 | EXPERIMENTAL

### 2.1 | Chemicals

Pluronic P123 (MW ~ 5800 g mol<sup>-1</sup>) was obtained from Sigma–Aldrich (Merck, Germany). Citric acid (≥99.5%, anhydrous), trisodium citrate dihydrate (≥99%), and sodium silicate (7.8–8.5 wt.% Na<sub>2</sub>O, 25.8–28.5 wt.% SiO<sub>2</sub>) were purchased from Carl Roth (Germany). Deionized water (DIW) was used for all syntheses and preparations. Bentonite, sodium form (NaBent) was purchased from Alfa Aesar (Thermo Fischer Scientific, Germany, Prod. Nr.: A15795), and Methocel F50 (MF50) was purchased from Dow Chemical Company (USA). Dolapix A88 was purchased from Zschimmer and Schwartz (Germany). Low viscosity silicon oil (Polydimethylsiloxane, 20 cSt at 25°C) was sourced from VWR Chemicals (USA).

### 2.2 | Synthesis of uncalcined COK-12

The synthesis of COK-12 was performed in a batch upscaled by a factor of 50 as previously reported.<sup>[44]</sup> Briefly, 200 g P123 was dissolved in 5375 mL DIW before 168.1 g anhydrous citric acid, 144.1 g trisodium citrate dihydrate, and a solution of 520 g sodium silicate in 1500 mL DIW were incorporated. After a day of aging at RT, the precipitated solids were filtered from the aqueous solution, washed with 25 L DIW, and dried at 60°C. The resulting powder was not calcined, hence the soft-template was still present.

### 2.3 | Mixing of robocasting slurries

Slurries for robocasting were prepared in three subsequent steps as follows: Given amounts (Table 1) of sodium bentonite (NaBent) as the inorganic binder, uncalcined COK-12 and Methocel F50 as an organic binder (MF50), were well mixed together using a rotary mixer (RW16 basic, IKA-Werke GmbH & Co. KG, Germany) until a homogeneous mixture was achieved.

Afterwards, a suitable amount of dispersant solution (Dolapix A88) was added to achieve a final proportion of 0.3 wt.% of dispersant, and the mixture was thoroughly mixed to ensure uniform coverage. Finally, DIW was slowly added and mixed for 5 minutes until a homogeneous slurry was formed. NaBent concentrations were chosen to explore reported compositions in the literature.<sup>[53]</sup>

The monolith obtained from NB-COK-25-P after calcination at 600°C is denoted as NB-COK-25-M. COK-12-600 and NaBent-600 refer to the calcined raw material. When referring to groups of samples, the labeling NB-COK-X(-P, -M) will be used.

### 2.4 | Robocasting of COK-12 monoliths

Suitable slurries were loaded into a transparent polypropylene (PP) syringe barrel (30 mL, Vieweg, Germany), with a Luer lock to which a 0.84 mm straight metallic dispensing tip (Vieweg, Germany) was connected. This barrel was then loaded onto an Ultimaker 2+ connect 3D printer (Ultimaker, Netherlands) with a modified print head that accommodates the PP syringe (Figure S1), as used in previous work.<sup>[54]</sup> Paste extrusion was achieved by employing pressurized air at varying pressures depending on the rheology of the slurry, commonly between 3 and 5 bar. The printing speed was 7 mm s<sup>-1</sup>, while the layer height was 0.5 mm. Printing was carried out at RT. The monoliths were fabricated in a layer-by-layer fashion in a simple cubic structure. All monoliths had a square cross-section of 20 × 20 mm<sup>2</sup> and 10 mm in height. The structures were designed in FreeCAD (Juergen Riegel, Werner Mayer, Yorik van Havre (2001–2017). FreeCAD (Version 0.19 [Software] Available from <http://www.freecadweb.org>), and the corresponding G-CODE for their printing was generated through a custom-made Python script.

The obtained structures were dried for 24–48 hours in a partially opened moisture-saturated desiccator to ensure a slow drying procedure, avoiding the formation of cracks. Once dried, the structures were calcined in a laboratory oven (K 114, Heraeus, Germany), from RT to 300°C

**TABLE 2** Summary of the slurry compositions and the NaBent to solids ratio used for the rheological studies. Slurries were formulated to 25% solid volume content.

Sample	Solids			Water (wt.%)	Liquids	
	NaBent to solids ratio <sup>a</sup> (%)	Uncalcined COK-12 (wt.%)	NaBent (wt.%)		MF-50 (wt.%)	Dispersant (wt.%)
NB-COK-25-S	24.6	27.1	8.9	62.8	0.9	0.3
NB-COK-18-S	18.2	29.0	6.4	63.4	0.9	0.3
NB-COK-13-S	13.4	30.3	4.7	63.8	0.9	0.3
NB-COK-0-S	0.0	33.9	0.0	64.9	0.9	0.3

<sup>a</sup>NaBent to solids ratio is defined as NaBent (wt.%) / (NaBent (wt.%) + uncalcined COK-12 (wt.%)).

in 10 hours (0.5°C min<sup>-1</sup>), 300°C to 600°C in 5 hours (1°C min<sup>-1</sup>), dwelling at 600°C for two hours and then allowed to reach RT by passive cooling.

## 2.5 | Characterization

The rheological properties of a set of synthesized slurries (Table 2) were first measured with an Anton Paar MCR-301 rheometer (Anton Paar, Austria) using a parallel plate PP50 accessory (diameter = 49.978 mm), prepared in the same manner as the ones for printing. To make valid comparisons, these slurries were formulated to a constant 25% solid volume content and are denoted NB-COK-X-S, where X is the approximate NaBent to solids ratio.

The rheological parameters of the produced slurries were determined by two different kinds of measurements, flow curves and (stress) amplitude sweeps. These two measurements differ in the type of stress applied (continuous vs. oscillatory), and complement each other to generate a complete report on the slurry's behavior when printing.<sup>[53]</sup>

Flow curves were obtained from exponentially spaced shear rate sweeps from 100 s<sup>-1</sup> to 0.01 s<sup>-1</sup>. Oscillating amplitude sweeps were obtained from a logarithmically spaced strain amplitude of 0.01 to 100% and a frequency of 1 Hz. A dome-like accessory was used to prevent excessive solvent evaporation, and the edge of the parallel plate was slightly brushed with low viscosity silicon oil to further impede the evaporation of water. A pre-shear period at a constant shear rate was applied to all samples until constant viscosity was reached to ensure the reproducibility of results. The results were obtained by averaging the fit results of 5 curves. Flow curve results were fitted to the Herschel–Bulkley (HB) model shown in Equation (1), from 0.5 s<sup>-1</sup> to 100 s<sup>-1</sup>, due to strong variations of the results at lower rates.  $\sigma$  is the measured shear stress,  $\sigma_{y,HB}$  [Pa] is the yield stress obtained from the HB model,  $K[\text{Pa}\cdot\text{s}^{-n}]$  is the consistency factor,  $\dot{\gamma}$  is the shear rate, and  $n$  is the flow index.

$$\sigma = \sigma_{y,HB} + K\dot{\gamma}^n \quad (1)$$

The linear viscoelastic storage modulus ( $G'_{LVER}$  [Pa]) was obtained from the constant portion of the amplitude sweep at low Shear strain, inside of the linear viscoelastic range (LVER). Data were statistically analyzed with the Dixon's Q test for outliers at a 95% confidence level. Outliers were excluded from the fit.

To calculate the Feilden printability ( $\phi_F$ )(2)<sup>[1]</sup> and the flow transition index (3),<sup>[36]</sup> the stresses calculated from the intersection of the storage modulus ( $G'$ ) and the loss modulus ( $G''$ ) curves (Flow stress,  $\sigma_f$ ) and the stress corresponding to the end of the LVER (Yield stress as measured by the amplitude sweep method,  $\sigma_{y,LVER}$  were used).<sup>[25]</sup>

$$\phi_F = \frac{G'_{LVER}}{\sigma_f} \quad (2)$$

$$FTI = \frac{\sigma_{y,LVER}}{\sigma_f} \quad (3)$$

The sintering behavior of the printed slurries and thermal decomposition of their contents (e.g., uncalcined COK-12 soft-template, organic (MF-50) and inorganic binders (i.e., NaBent)) was examined by thermogravimetric analysis, coupled with a mass spectrometer (TGA-MS) in air using an STA 409 PC LUX (Netzsch, Germany) and a PFEIFFER OMNISTAR GSD320 O1 (Pfeiffer Vacuum GmbH, Germany), equipped with an iridium filament and heated lines. The measurements were carried out from RT to 600°C with a 15°C min<sup>-1</sup> ramp, under a synthetic air atmosphere (N<sub>2</sub>:O<sub>2</sub> 80:20) with ca. 35 mg of sample. Signals at 18 and 44 m/z were the only ones tracked with MS.

Slurry pH was measured with “pH-Fix 0-14” color fixed indicator strips (Macherey-Nagel, Germany).

Powder XRD measurements were performed using a D8 ADVANCE x-ray diffractometer (Bruker AXS GmbH, Germany) equipped with a Lynx Eye 1D detector with a copper radiation source ( $\lambda$  (K $\alpha$ ) = 1.542 Å). The measurements were carried out in a Bragg-Brentano geometry and a divergence slit of 0.5°. The  $2\theta$  angles from 10° to 80° were collected in 0.020° increments with 1 s per increment at RT. Samples were ground with an agate mortar before the XRD was conducted.

Micro-Computed Tomography ( $\mu$ CT) measurements of calcined whole monoliths were performed in an EasyTom 160 (RX solutions, France) equipped with a tungsten filament micro tube x-ray source (L12161-07, Hamamatsu Photonics K.K, Japan). Detection was carried out with a flat panel detector (CsI scintillator, Active pixel area: 1874\*1496 pixels) and a Cu filter. In each measurement, the applied tube voltage was 100 kV, the current 100  $\mu$ A, the power 10 W, and the total measurement time was 84 minutes, resulting in a 3D map with a voxel size of  $15 \times 15 \times 15 \mu\text{m}^3$ . The resulting images were analyzed with Dragonfly (ORS, Canada). In detail, length measurements for the shrinkage and strut axes were obtained from the distance measuring tool taking 5 measurements of each distance at different layers and positions on the monolith. Strut perimeter and area were calculated by fitting an ellipse on the strut cross-section and calculating the corresponding perimeter and area, considering 10 different struts in different monolith sections. Porosity was calculated by bounding the center of the structure with a  $10 \times 10 \times 4 \text{ mm}^3$  box (shortest dimension in the printing direction), then selecting all the voxels corresponding to the structure and dividing them by the total amount of voxels in the bounding box.

The pore structure, pore size, and SSA of printed, calcined and cut (using an M3400 diamond wire saw (Well Diamantdrahtsäge GmbH, Germany)) monoliths were studied by nitrogen sorption analysis in a QuadraSorb Station 4 apparatus (Quantachrome, USA). Isotherms were recorded at 77 K after degassing for 12 hours at 200°C under vacuum. The surface area was determined using the Brunauer, Emmet, and Teller (BET) method utilizing the Rouquerol criteria. The estimation of the size of the mesopores was based on NLDFT (Adsorption branch) for COK-12 and mixtures and BJH (Barrett–Joyce–Halenda) calculations using the adsorption branch of the isotherm in the case of NaBent-600 sample. All nitrogen sorption data were analyzed using the QuadraWin (Anton Paar QuantaTec Inc.) software.

SAXS data on COK-12-600, NaBent-600 and calcined monolith pieces were collected using the MOUSE instrument, using a microfocus monochromatized x-ray source Cu  $K\alpha$  ( $\lambda = 0.154 \text{ nm}$ ).<sup>[55]</sup> Data was collected using an in-vacuum Eiger 1 M detector (Dectris, Switzerland) placed at multiple distances between 57 and 2507 mm from the sample. Powder (COK-12-600 and NaBent-600) and pieces of monolithic samples (NB-COK-X-M) were held in the beam between two pieces of Scotch Magic tape. The resulting data were processed using the DAWN software package using standardized data correction procedures.<sup>[56,57]</sup> Fitting of the SAXS data was performed using the SASfit software package, utilizing a previously reported fitting model for COK-12 samples.<sup>[42,44,58]</sup> The data collected on

NaBent was modeled using a spherical formfactor alongside a flat background contribution and a Porod slope. NB-COK-X-M samples were modeled using a combination of both aforementioned models to account for contribution arising for both structures.

Wall thickness,  $W_t$ , was calculated from the data according to Equation (4):

$$W_t = a_0 - d_p \quad (4)$$

Where  $a_0$  is the obtained lattice parameter from SAXS measurements, and  $d_p$  is the pore diameter, obtained from both NLDFT or SAXS analysis.

In addition, the wall area ( $W_a$ ) of the system was calculated, as follows:<sup>[36]</sup>

$$W_a = \frac{\sqrt{3}}{4} a_0^2 - \frac{\pi}{8} d_p^2 \quad (5)$$

The compressive strength of the thermally treated monoliths was examined based on ISO 17162:2014.<sup>[59]</sup> Therefore, the 3D-printed monoliths were cut into cuboids of ca.  $4 \times 4 \times 8 \text{ mm}^3$  using the previously described diamond wire saw. Four samples per parameter set were tested in a universal testing machine Z020 (ZwickRoell, Germany) equipped with a 20 kN load cell under a loading rate of  $0.75 \text{ N s}^{-1}$ . Monoliths were compressed perpendicular to the printed layer plane. Stress to fracture was calculated by dividing the force recorded before the first significant drop by the area of the tested probe's face. The Apparent Young's Modulus ( $E$ ) was calculated from the linear correlation between stress ( $\sigma$ ) and strain ( $\epsilon$ ) as  $\sigma = E\epsilon$ .

## 3 | RESULTS AND DISCUSSION

### 3.1 | Slurry rheological behavior

#### 3.1.1 | Flow behavior under continuous stress

The rheology of slurries with different compositions (Table 2) was measured and analyzed using the Herschel–Bulkley (HB) model and found to be shear-thinning in all cases. Fitted parameters (Table 3), except the flow index, show a non-linear dependence with NaBent content and are shown in Figure 1. Average flow curves are shown in Figures S3 and ID).

The obtained yield stress ( $\sigma_{y,HB}$ ) increases in tandem with the NaBent content of the slurries (Figure 1A). The behavior of such colloidal fluids under stress can be explained by a transition between two structures.<sup>[60]</sup> The first structure at rest (or at a stress  $\sigma < \sigma_{y,HB}$ ), where there is no actual flow and therefore no viscous forces,

**TABLE 3** Rheological parameters resulted from fitting the experimental data for different slurry compositions, showing that a decrease in the flow index resulted in markedly increased shear thinning behavior.

Sample	$\sigma_{y,HB}$ (Pa)	$K$ (Pa.s <sup>-n</sup> )	$n$	$\sigma_f$ (Pa)	$G_{LVER}'$ (Pa)	$\sigma_{y,LVER}$ (Pa)
NB-COK-25-S	259	95	0.32	86	20087	17
NB-COK-18-S	148	66	0.35	68	16578	11
NB-COK-13-S	160	87	0.50	43	21401	6
NB-COK-0-S	96	34	0.69	41	44068	13

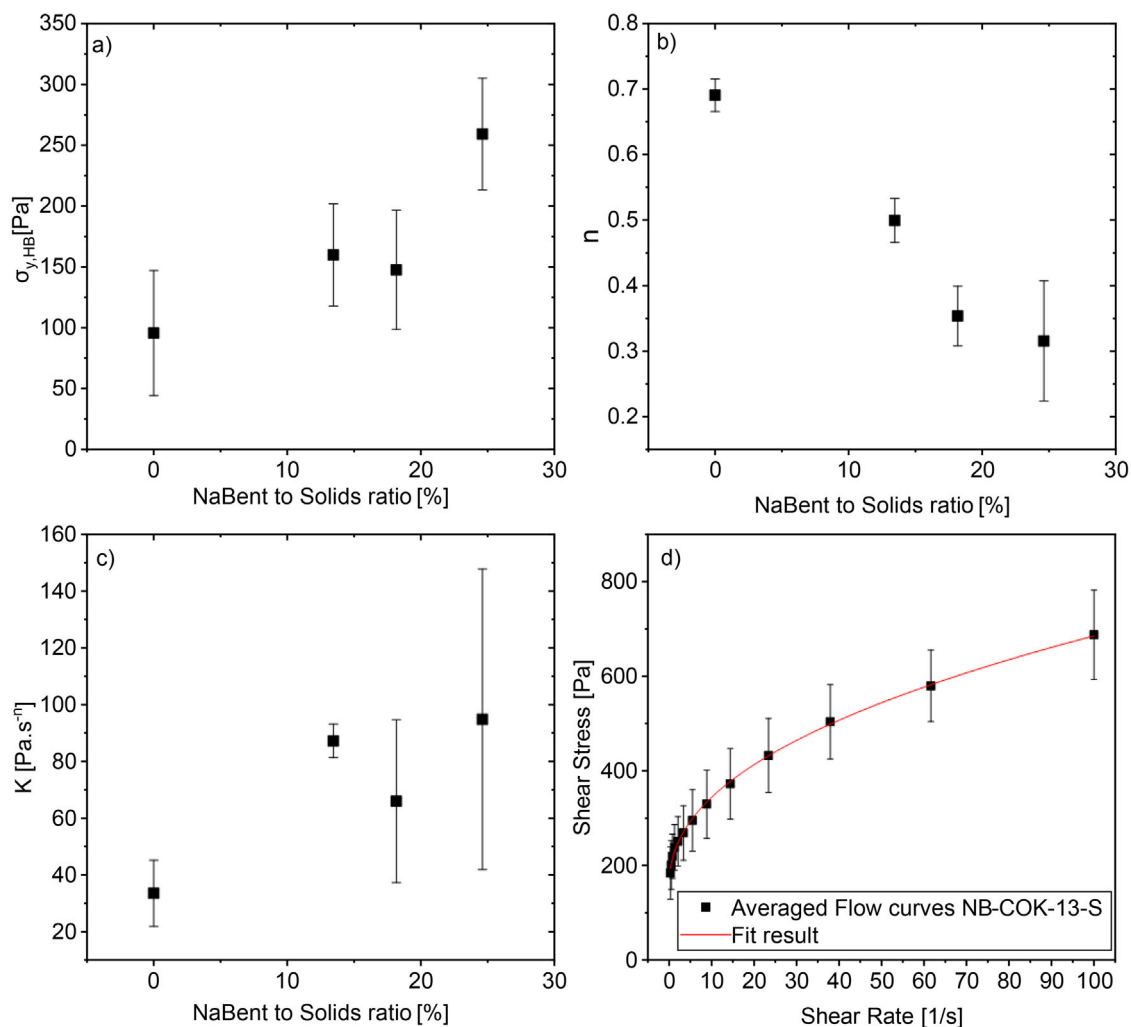


**FIGURE 1** A, Hershel-Bulkley yield stress ( $\sigma_{y,HB}$ ), (B) flow index ( $n$ ), and (C) consistency factor ( $K$ ) as a function of NaBent to solids ratio for samples NB-COK-X-S. ( $X = 0, 13, 18, 25$  representing NaBent to solids ratio). D, Average of 5 flow curve measurements for NB-COK-13-S and best fit curve according to the Hershel-Bulkley model (fitting parameters are shown in Table S1).

is dominated entirely by “cohesive forces” between the randomly oriented particles in suspension. The second structure, during the transition to high shear rates, where viscous forces prevail over the interparticle forces and flow begins and reaches a very high shear limit, where the structure is completely controlled by hydrodynamic effects. Accordingly, the growth in yield stress indicates a more stable pre-flow configuration. This could be due to an increase in the magnitude of the interparticle

forces (i.e., the COK-12/COK-12 interactions are of lower magnitude than the COK-12/NaBent interactions).

The impact of the composition changes on the flow index ( $n$ ) obtained from the Hershel-Bulkley model fit can be seen in Figure 1B. The trend is expectedly non-linear, and the flow index decreases with NaBent content. The flow index is related to the new structural arrangement under shear, and pastes with a flow index lower than one is referred to as “shear thinning”. Adding NaBent increases

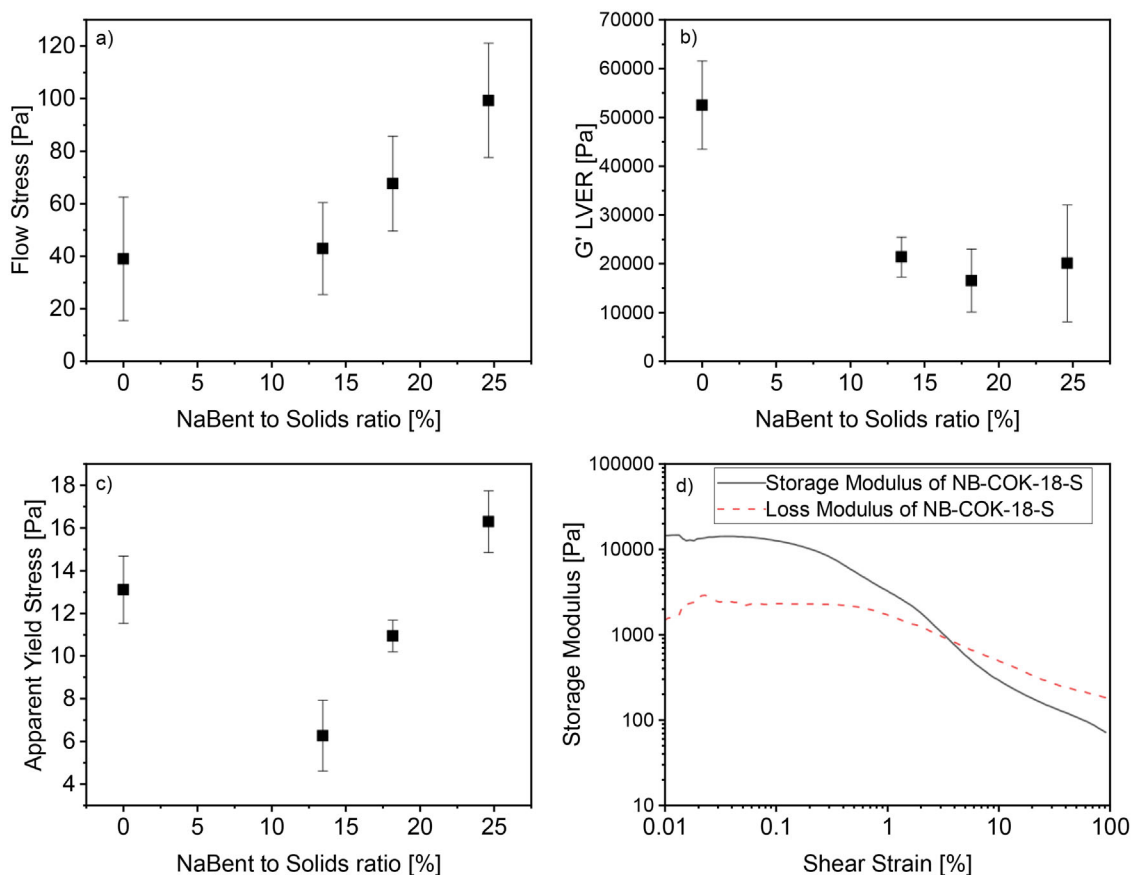


**FIGURE 2** A, Flow stress ( $\sigma_f$ ), (B) stiffness ( $G'_{LVER}$ ), and (C) yield stress as measured per the amplitude sweep method ( $\sigma_{y,LVER}$ ) as a function of NaBent to solids ratio for slurry compositions NB-COK-X-S (X = 0, 13, 18, 25 representing NaBent to solids ratio). D, Measurement results for an amplitude sweep on the slurry composition NB-COK-18-S.

the slurry's shear-thinning behavior, making it easier to extrude. The already existing shear thinning behavior of NB-COK-0-S can be attributed to an alignment of COK-12 with slightly anisotropic particles under flow, the breakage of agglomerates under shear, and the disentanglement of the polymer chains of the MF-50. The slurries (except for NB-COK-0-S) contain NaBent binder with sodium montmorillonite as a main component. Sodium montmorillonite is known for its smectite-type layered configuration, which is very anisotropic and contributes to the "ordering" of this flow structure, reducing its resistance to deformation. The last fitted parameter, the consistency coefficient ( $K$ ), does not show a clear trend, although the variations are rather small. As a final comment on the statistical uncertainty of the results, it is possible that the increasing binder content is causing some kind of thixotropic behavior (i.e., a delayed response of the system to changes in shear), which would incorporate some systematic error.

Figure 1D exemplifies the results obtained, showing the averaged data series for NB-COK-13-S and the best-fitting curve to the HB model (Detailed fit parameters found in Table S1).

### 3.1.2 | Flow behavior under oscillating stress

Figure 2 shows trends resulting from the analysis of amplitude sweep curves (flow stress,  $\sigma_f$ ,  $G'_{LVER}$ , also called "stiffness", and the yield stress as measured by the amplitude sweep method ( $\sigma_{y,LVER}$ )<sup>[61]</sup>).  $G'_{LVER}$  is related to the forces at rest in the slurries in a manner similar to the yield stress, while the flow stress represents the stress at which there is a transition from a deformed solid-like substance to a flowing liquid-like behavior (known as the solid-to-fluid transition). These seem to follow opposite trends, which indicates that the addition of binder generates slurries that are easier to deform (less stiff) but harder to put into a flow state. Finally,  $\sigma_{y,LVER}$  is another measure of the yield stress that should correspond, in theory, to the same physical quantity as  $\sigma_{y,HB}$ . However, these values show a discrepancy in both absolute value and the overall trend compared to the previously obtained by fitting the flow curves (Figure 1, Figure S3). The discrepancy between the yield stress obtained by fitting the flow curves by the HB model and the one given by the analysis of the Amplitude sweep curves is noted in the literature.<sup>[25,27]</sup> This discrep-

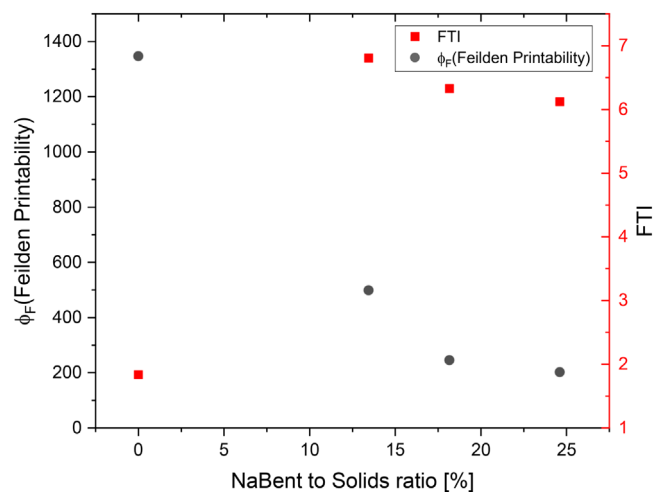


**FIGURE 3** Feilden Printability ( $\phi_F$ ) and flow transition index (FTI) as a function of NaBent to solids ratio for NB-COK-X-S (X = 0, 13, 18, 25 representing NaBent to solids ratio). The slurry is generally considered printable if  $\phi_F > 20$  and FTI < 20.

ancy is due to the fact that both the flow curve approach (continuous stress) and the amplitude sweep (oscillating stress) probe different stress ranges at different time scales and with different resolutions. Additionally, the intersection method (actually, all methods) of determining  $\sigma_{y,LVER}$  leaves room for some ambiguity.<sup>[25]</sup> It bears noting that for both kinds of results, the compositions analyzed produce results whose magnitude is in line with what is expected in the literature.<sup>[1,27,61]</sup> Finally, the  $\sigma_f$  trend is in good agreement with the  $\sigma_{y,HB}$  in Figure 1A. These two quantities are unambiguously defined (The first as the  $G'-G''$  intersection, the other as the result of the fit).<sup>[25]</sup> This corroborates the idea that  $\sigma_{y,HB}$  better describes the situation close to the transition point, and the stiffness and  $\sigma_{y,LVER}$  better reflect the forces at low shear, far from  $\sigma_f$ . As such, the decrease in stiffness and  $\sigma_{y,LVER}$  might be due to a deficient packing of the rest structure when NaBent is present (given their shape mismatch), leading to higher interparticle distances and lower cohesive forces. When under stress ( $\sigma_{y,LVER} < \sigma < \sigma_f$ ), the system transitions into a structure that then resembles the situation under flow conditions.

### 3.1.3 | Printability

The ratio between  $G_{LVER}'$  and  $\sigma_f$  (Feilden Printability,  $\phi_F$ ) has been adopted by Feilden<sup>[1]</sup> as an indicator of “printability”, and further work by Corker used the flow transition index (FTI) as another indicator.<sup>[61]</sup>

Figure 3 shows the resulting calculation for the previously mentioned printability figures of merit,  $\phi_F$ , and FTI. As can be seen, all the compositions lie in the correct range to be considered as “printable” (defined as ratios of > 20

for  $\phi_F$  and < 20 for the FTI, although these ranges are not necessarily universal). However, a reduction in printability (i.e., a reduction of  $\phi_F$ , and an increase in FTI) is seen when the NaBent to solids ratio increases. It is important to mention that all printability figures arise from theoretical considerations and are ultimately not perfect descriptors of the printing process but rather establish reasonable boundaries to the slurry properties to predict adequate performance at a certain step of the printing procedure. In this case, minimizing the deflection of the printed part by the force imparted by the nozzle. A complete summary of the results for this section can be found in Table 3, where the results agree well with previously reported values for robot-casted slurries.<sup>[1]</sup> Although the rheological results show a reduction in the printability with using the bentonite content in the slurry, a high bentonite content is necessary to lower the processing temperature to avoid the loss of the mesoporosity and high surface area of COK-12 at sintering temperatures. Rheological measurements were also conducted for NB-COK-X-P samples, with similar conclusions for the printability results, as shown in Table S2.

## 3.2 | Thermal analysis

In order to determine the parameters of the thermal treatment necessary to eliminate the organic template while maintaining the porosity and maximizing the mechanical properties, as well as the approximate sample composition after it, TGA-MS measurements were conducted on NB-COK-25-P, uncalcined COK-12, and NaBent. A slight initial weight loss of sample NB-COK-25-P can be seen between 30°C–150°C accompanied by the evolution of water ( $m/z = 18$ ), indicating the loss of physically adsorbed moisture (Figure 4A). Similar behavior can also be seen for both bare materials, NaBent and COK-12 (Figure 4B,C), respectively). A larger weight loss is observed at 180°C–400°C for both in NB-COK-25-P and the uncalcined COK-12, which is accompanied by evolution of water ( $m/z = 18$ ) and  $\text{CO}_2$  ( $m/z = 44$ ), suggesting thermo-oxidative decomposition of the organic template in the COK-12, Pluronic P-123.<sup>[39]</sup> Moreover, a slight weight loss is observed above 600°C for the NB-COK-25-P sample, which can be attributed to the dehydroxylation of the surface silanol groups present in COK-12 and NaBent and to the decomposition of some existing organic material in NaBent.<sup>[62]</sup> The final weights of NB-COK-25-P, NaBent and uncalcined COK-12 after calcination are 49%, 83% and 55% of the original mass, respectively, leading to final monolith compositions detailed in Table 4.

Although these results suggest that the removal of the organic template forming a mesoporous network of COK-12 can be successfully done at calcination temperatures



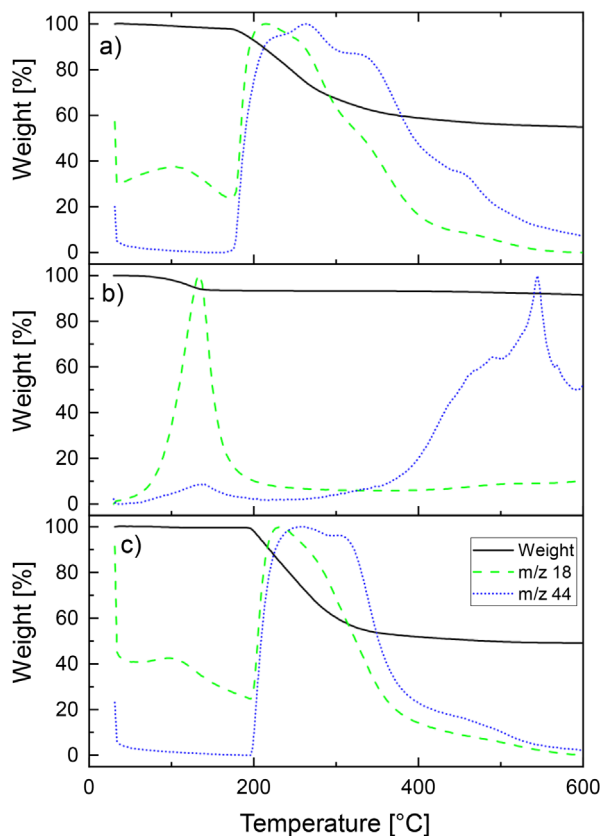


**FIGURE 4** TGA and normalized MS curves of NB-COK-25-P (A), NaBent (B), and COK-12 (C) materials showing weight loss and gas evolution during conditions similar to the thermal treatment of the printed parts (i.e., atmosphere: 80:20 N<sub>2</sub>:O<sub>2</sub>, heating rate: 15°C min<sup>-1</sup>).

**TABLE 4** Estimated final compositions of NB-COK-X-M calculated with the weight loss measured for the raw materials after thermal treatment. (49% for uncalcined COK-12 and 83% for sodium bentonite).

Sample	COK-12 (wt.%)	NaBent (wt.%)
NB-COK-25-M	64.1	35.9
NB-COK-18-M	72.8	27.2
NB-COK-13-M	79.3	20.7

around 350°C, higher sintering temperatures might be required to enhance the mechanical properties of COK-12 monoliths. Correlating with experimental observations, calcining the monoliths at temperatures lower than 600°C yields highly hydrophilic monoliths that will completely disaggregate in water. Notably, calcining past this temperature yields a mechanically stable monolith, which is still hydrophilic but will retain its structure even in the presence of boiling water and 2 atmospheres of pressure in an autoclave. It is possible that this higher cohesion force in the monoliths calcined at 600°C has its source in interparticle condensation reactions, which happen in

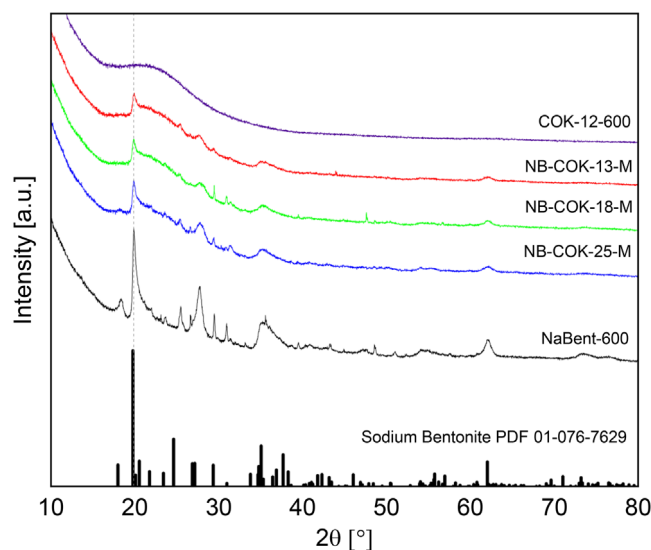


**FIGURE 5** X-ray diffractograms of calcined raw materials and NB-COK-X-M samples (X = 0, 13, 18, 25 representing NaBent to solids ratio). Dashed line at  $2\theta$  of 19.87° shows the position of the main reflection of sodium bentonite.

both materials (COK-12 and NaBent) in the same temperature range,<sup>[62,63]</sup> giving rise to Si-O-Si bridges between silanol groups in NaBent and COK-12 particles. This could be the reason for the stronger monoliths (Section 3.5) when calcining at 600°C, allowing for a process that conserves the mesoporous structure of the COK-12 (Section 3.6).

### 3.3 | Phase composition

XRD patterns of the calcined monoliths were taken to ensure the conservation of the amorphous structure of COK-12 after thermal treatment.

As seen in Figure 5, COK-12-600 appears amorphous, as indicated by the broad diffuse scattering peak at 20–25° without any defined reflections across the measuring range, which is in line with previous results.<sup>[44]</sup> NaBent-600 shows a pattern that can be well indexed with the reference pattern calculated for the monoclinic structure of sodium bentonite (PDF number 01-076-7629), with no extra reflections. Further information about this structure can be found elsewhere.<sup>[62]</sup> NB-COK-X-M samples (X = 0, 13, 18, 25 representing NaBent to solids ratio) show an expected mixture of the diffractograms of the calcined starting materials. With increasing binder content, the main reflection at 19.87° corresponding to the (020) planes of sodium montmorillonite becomes more prominent, while the broad diffuse scattering reflection of COK-12-600 becomes smaller. No significant phase changes were observed. These results confirm the conservation of the

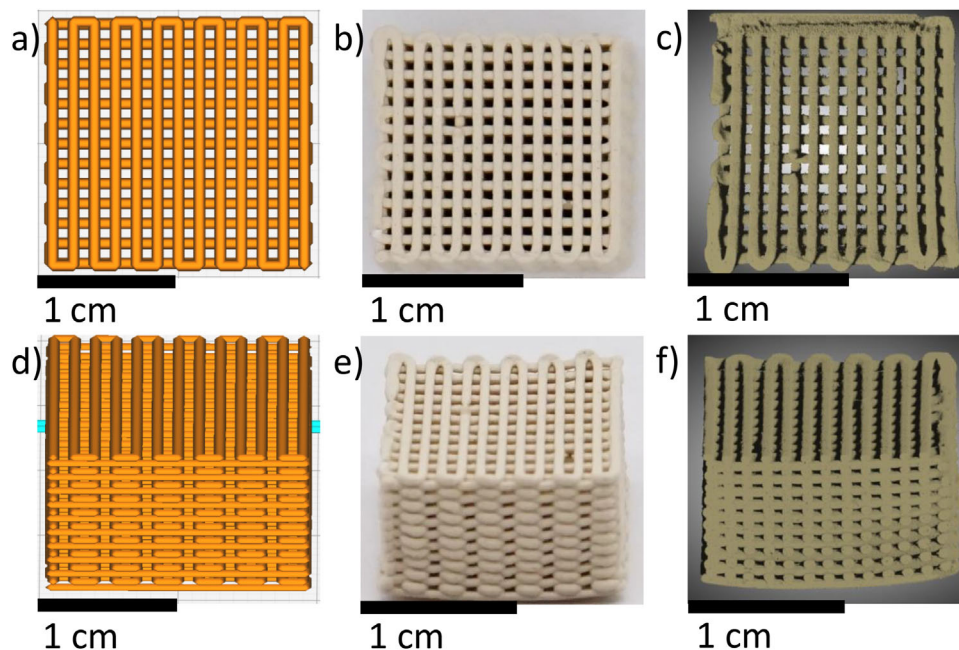


**FIGURE 6** A, Computer assisted design (CAD) model of a simple cubic woodpile structure, seen from the top. B, Top-view optical photo of printed NB-COK-25-P after calcination. C, micro-CT reconstruction of NB-COK-25-M monolith after calcination seen from the top. D, CAD model pictured in (A), from the side. E, Side-view optical photo of printed NB-COK-25-P after calcination. F, Micro-CT reconstructions of printed NB-COK-25-M monolith, with a top-to-bottom cut that shows the conserved internal channel structure of the monolith (ca.  $15 \times 15 \times 8 \text{ mm}^3$ ). Further details about the structure can be seen in Video S1.

amorphous and crystalline structures of the COK-12 and sodium bentonite, respectively, in the sintered monoliths.

### 3.4 | Morphology and geometry

To measure the difference between the designed and the printed monolith, micro-CT experiments were carried out. These experiments provide an accurate 3D representation of the printed monoliths and enable the measurement of their interior. We were unable to measure monoliths without sodium bentonite binder due to their low mechanical resistance.

Figure 6 shows in detail the geometry of the design model and the corresponding printed monolith before and after the calcination process. Samples have, by design, a structural porosity of 61% which was calculated by subtracting the design model from its bounding box in FreeCAD. Several measurements were performed on the printed bodies, which show consistency among their results and are displayed in Table 5. Linear shrinkage from model to post-calcination monolith is calculated to be 26%, 25%, and 25%, and geometric porosity is calculated to be 56%, 49%, and 52% for the NB-COK-13-M, NB-COK-18-M, and NB-COK-25-M monoliths, respectively with increasing binder content. Similarly, the cross-section of the struts is smaller than the nozzle cross-section ( $0.59 \text{ mm}^2$ ). The

amount of linear shrinkage is related to the water volume loss of NaBent during thermal treatment.<sup>[64]</sup> Figure 6F shows good contact between monolith layers, with good adhesion and some internal porosity, probably due to some micro air bubbles remaining during the mixing process. The internal structure looks well-conserved, and there does not appear to be any significant deformation of the struts, even when suspended. A small curvature on the bottom surface of the monoliths appears due to the difference in drying rate between the exterior and interior layers, leading to stresses. Remarkably, even though the uncalcined COK-12 loses over half of its mass during the calcination procedure, no significant cracks are observed after the calcination. The printed structures were similar for all compositions, as shown in Figure S2. Further details about the structure can be seen in Video S1.

### 3.5 | Mechanical properties

An uniaxial compression test was used to measure the compressive strength of the monoliths with different binder contents. Monoliths without NaBent could not be measured due to their low mechanical resistance.

As seen in Figure 7, the compressive strength increases with the amount of NaBent in the slurry. The obtained values were  $0.20 \pm 0.07 \text{ MPa}$ ,  $0.32 \pm 0.05 \text{ MPa}$ , and

**TABLE 5** Measured and calculated quantities from  $\mu$ CT results.

Sample	Strut perimeter (mm)	Strut area (mm <sup>2</sup> )	Strut ratio <sup>a</sup>	Porosity (%)	Linear shrinkage (%)
NB-COK-13-M	1.93 $\pm$ 0.05	0.29 $\pm$ 0.02	0.86 $\pm$ 0.03	56.37	25.95
NB-COK-18-M	1.99 $\pm$ 0.06	0.31 $\pm$ 0.02	0.84 $\pm$ 0.07	48.82	24.66
NB-COK-25-M	1.80 $\pm$ 0.06	0.26 $\pm$ 0.02	0.85 $\pm$ 0.04	51.90	24.83

<sup>a</sup>Ratio of the length of the minor axis to the length of the major axis.

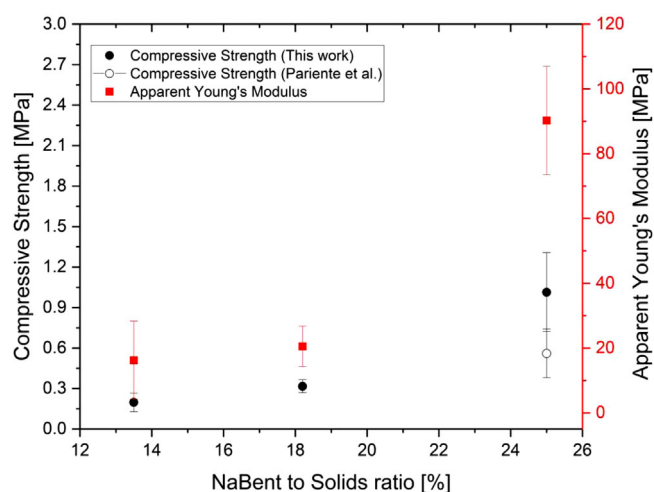


**FIGURE 7** Compressive strength and apparent Young's modulus of NB-COK-X-M (X = 0, 13, 18, 25 representing NaBent to solids ratio) as a function of used NaBent content. The open circle symbol denotes reference work from Pariante et al.<sup>[66]</sup>

1.0  $\pm$  0.3 MPa for the NB-COK-13-M, NB-COK-18-M, and NB-COK-25-M, respectively (Stress-strain curves in Figure S5). This monotonically increasing relationship was expected. A similar trend for the apparent Young's modulus can also be observed. These results can be explained by the increase in the number of binding interactions between COK-12 and NaBent as their amounts increase in the monoliths, which agrees with previous work reported for extrudates of OMS.<sup>[65]</sup> In particular, a similar composition to NB-COK-25-M was explored by Pariante et al., yielding a range of 0.56  $\pm$  0.18 MPa for the corresponding compressive strength.<sup>[65,66]</sup> Remarkably, the presented monoliths here achieve a similar mechanical strength while having a higher SSA. The observed mechanical strength trend does not appear to be linear. It is important to remark that these results are influenced by the monolith shape, which is very porous and only represents the performance of the material in this shape.

### 3.6 | Porous structure

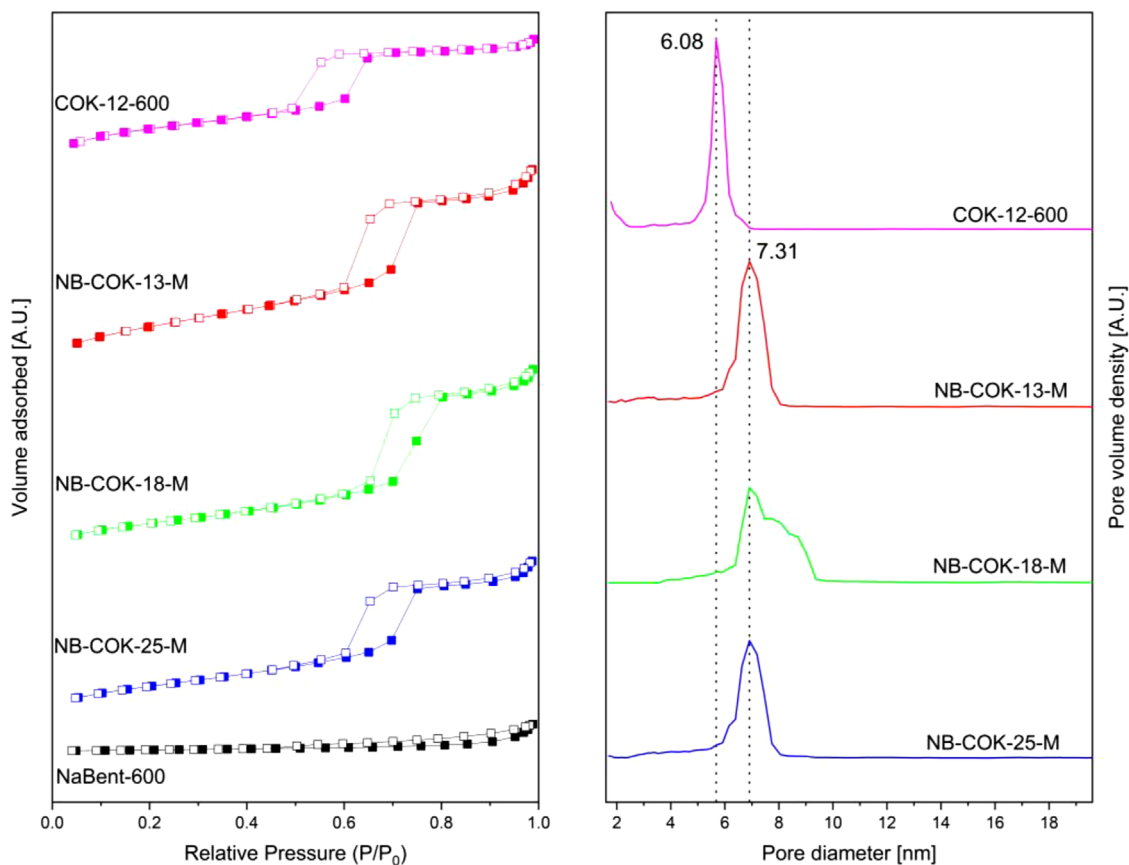
Figure 8A shows nitrogen sorption isotherms of NB-COK-X-M and calcined raw materials. The COK-12-600 isotherm shows a type IV(a) isotherm with a typical H1 hystere-

sis loop, as reported previously for mesoporous materials with cylindrical shapes.<sup>[44]</sup> The NaBent-600, the other main component of the samples, shows a type III isotherm with an H3 hysteresis loop, typical for clays with plate-like aggregates.<sup>[67]</sup> The monoliths show a type IV(a) isotherm with a type H1 hysteresis loop, suggesting a conserved pore shape.

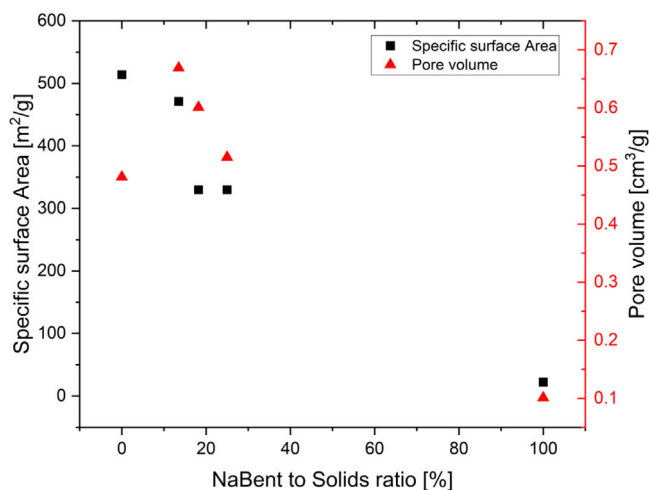
When compared to COK-12-600, a lower initial specific adsorbed volume can be seen in all cases (Figure S6). Moreover, NB-COK-13-M has a higher specific adsorbed volume than NB-COK-18-M and NB-COK-25-M. This could be interpreted as a progressive loss of microporous volume with increasing NaBent content. All samples have their hysteresis onset at higher relative pressures when compared to COK-12-600, suggesting bigger mesopores. This is backed by NLDFT calculations, shown in Figure 8B, where we see consistently bigger pores in the NaBent-containing samples in comparison with COK-12-600. The distributions change not only in average but also in width, with the NB-COK-X-M having a wider distribution than the COK-12 reference. The reference also shows a detectable smaller pore population in the micropore range, absent in the monoliths. Figure 9 shows the specific pore volume for the samples and calcined raw materials calculated through NLDFT. Although the specific pore volume of NB-COK-13-M monolith is significantly higher than that of COK-12-600, a decrease in the pore volume is observed with further increasing the NaBent content. This decrease in the pore volume at higher content of NaBent is expected due to the lower specific pore volume of NaBent. It is important to note that these quantities are subjected to some systematic error due to the NLDFT model used being set up with pure silica nitrogen sorption isotherms as its basis functions.

Figure 9 shows the variation of the BET-calculated SSA with the NaBent content of the monoliths. The figure also includes the resulting SSA for the COK-12-600 and NaBent-600. As expected, the SSA decreases with an increase in the NaBent content due to the low SSA of NaBent itself.

SAXS measurements were performed to gain insights into the structural changes occurring upon altering the ratio of NaBent to COK-12. SAXS curves for each NB-COK-X-M sample were measured and are shown in Figure 10, and their model fit results are shown in Figure 11.



**FIGURE 8** Results of Gas sorption measurement for the calcined bare materials and monoliths. A, Nitrogen sorption isotherms of calcined raw materials (COK-12-600 and NaBent-600) and samples NB-COK-X-M ( $N_2$  physisorption @77 K). Open symbols represent the desorption branch of the isotherm. All curves have an offset. B, Pore size distributions calculated by NLDFT. The surface is assumed to be composed entirely of silica, and the pores are assumed to be cylindrical. Reference lines added at 6.08 nm and 7.31 nm, the modal pore diameters for the COK-12-600 and the samples, respectively. All curves have an offset.



**FIGURE 9** BET surface area and NLDFT pore volume of NB-COK-X-M (X = 0, 13, 18, 25 representing NaBent to solids ratio) as a function of the NaBent (Binder) content. 0 and 100% are COK-12-600 and NaBent-600. NaBent-600 pore volume was calculated through BJH.

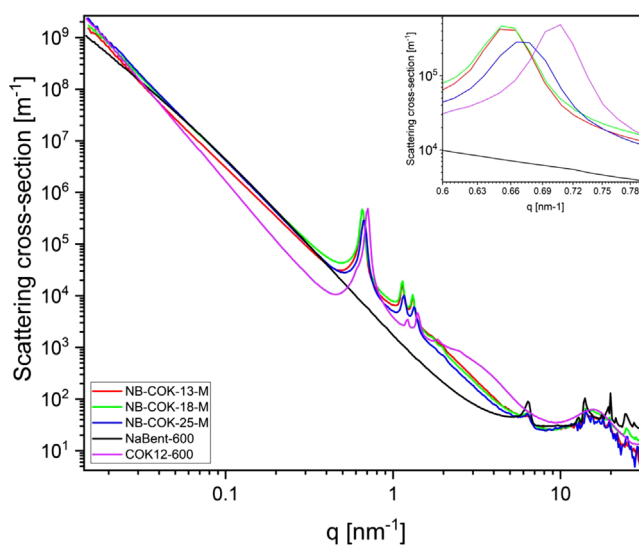


**FIGURE 10** SAXS curves in the 0.1 to 37.5  $nm^{-1}$   $q$  range of NB-COK-X-M (X = 0, 13, 18, 25 representing NaBent to solids ratio) and reference materials. Inset: Closeup of the 0.6 to 0.8  $nm^{-1}$   $q$  range.

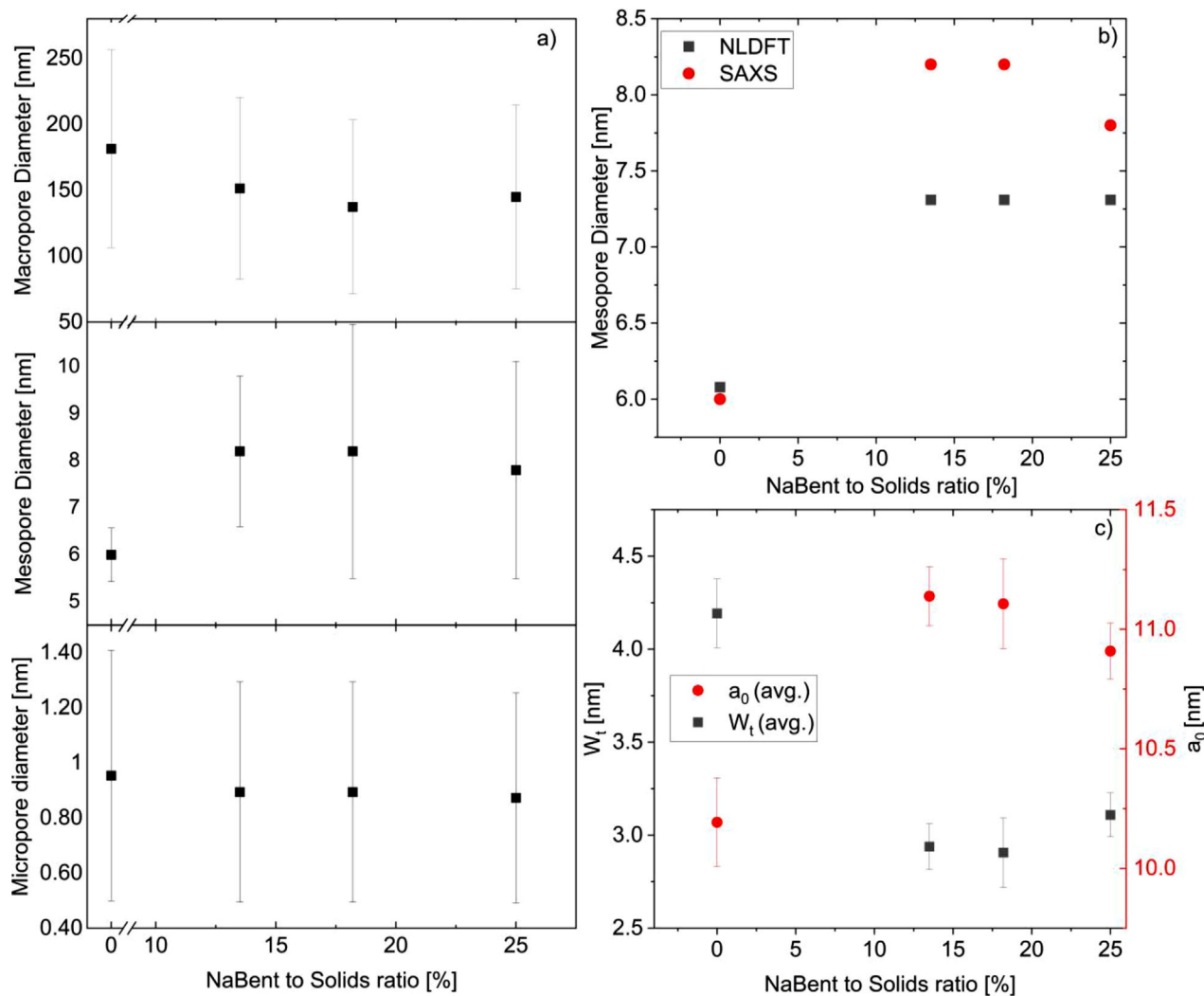


**FIGURE 11** Summary of SAXS pore distribution model fit results, lattice parameter ( $a_0$ ) and COK-12 wall thickness ( $W_t$ ). A, Micro, meso, and macropore diameter model fit output for COK-12 pore populations for NB-COK-X-M (X = 0, 13, 18, 25 representing NaBent to solids ratio) samples. The square symbols in the graph represent the average of the distribution, while the bars represent its standard deviation. B, Discrepancy in mesopore diameter of the COK-12 pore populations between NLDFT and SAXS modeling. C, Average cell parameter and wall thickness calculation results derived from SAXS curves. Bars represent the total difference between the two results.

At high  $q$ , COK-12-600 exhibits a broad peak consistent with the amorphous silica structure of COK-12 (sub-nm). COK-12-600 and NB-COK-X-M monoliths exhibit three well-resolved reflections between  $0.5 < q < 2 \text{ nm}^{-1}$ , consistent with  $P6m$  hexagonal symmetry ( $q_1:q_2:q_3 = 1:\sqrt{3}:2$ ).<sup>[68]</sup> These peaks are then assignable to the reflections with Miller indices (10), (11), and (20) of the hexagonal lattice. The position of the (10), (11), and (20) reflections for each sample, while consistent with a hexagonal lattice, are not perfectly matching to the predicted positions with small deviations from a geometrically perfect hexagonal lattice. Our analysis for the derived quantities considers this, generating two data series, as seen in Table 6 and Figure 11C, which are discussed further in this section. The (10) reflection shows a shift towards lower  $q$  when com-

paring COK-12-600 and the NB-COK-X-M samples, which translates to a hexagonal ordering with longer distances between vertices.

One result of the model fit is a set of pore size distributions for the micro-, meso- and macro- porosity for the COK-12 component of the mixture and a set of pores for the NaBent component of the mixture.

Figure 11A shows the model fit results for the micro, meso, and macro porosity of the COK-12 component of the model as a function of the final NaBent content. The square symbols in the graph represent the average of the distribution, while the bars represent its standard deviation. In all cases, the pore distribution for the NaBent-containing samples differs from that of the COK-12-600 reference. In particular, for the macropores, the trend shows a ca. 20%

**TABLE 6** Summary of measured properties of samples, reference SBA-15 materials, and related literature data.

Sample	$S_{\text{BET}}^a$ ( $\text{m}^2/\text{g}_{\text{ads}}$ )	$\bar{V}_{\text{pore}}^b$ ( $\text{cm}^3/\text{g}_{\text{ads}}$ )	$S_{\text{BET,SiO}_2}^c$ ( $\text{m}^2/\text{g}_{\text{SiO}_2}$ )	$\bar{V}_{\text{pore,SiO}_2}^c$ ( $\text{cm}^3/\text{g}_{\text{SiO}_2}$ )	$d_{\text{p,NLDFT}}$ (nm)	$d_{\text{p,SAXS}}^e$ (nm)	$a_{0,\text{PL}}^f$ (nm)	$a_{0,\text{RL}}^f$ (nm)	$W_{\text{t,PL}}^g$ (nm)	$W_{\text{t,RL}}^g$ (nm)	$W_{\text{a,PL}}^j$ ( $\text{nm}^2$ )	Ref.
COK-12-600	514	0.481	514	0.481	6.08	6.0	10.1	10.28	4.1	4.28	30.03	TW
NB-COK-13-M	471	0.669	606	0.861	7.31	8.2	11.2	11.01	3.0	2.81	27.91	TW
NB-COK-18-M	330	0.601	466	0.849	7.31	8.2	11.2	11.08	3.0	2.88	27.91	TW
NB-COK-25-M	330	0.515	535	0.835	7.31	7.8	10.9	10.97	3.1	3.17	27.08	TW
Na-BENT-600	22	0.101 <sup>h</sup>	–	–	–	–	–	–	–	–	–	TW
SBA	–	0.74 <sup>h</sup>	–	0.74 <sup>h</sup>	6.6 <sup>h</sup>	–	10 <sup>i</sup>	–	3.7	–	–	[70]
B-SBA-Be9	–	0.64 <sup>h</sup>	–	0.70 <sup>h</sup>	6.6 <sup>h</sup>	–	10 <sup>i</sup>	–	3.7	–	–	[70]
B-SBA-Be17	–	0.63 <sup>h</sup>	–	0.76 <sup>h</sup>	6.7 <sup>h</sup>	–	10 <sup>i</sup>	–	3.6	–	–	[70]
B-SBA-Be33	–	0.49 <sup>h</sup>	–	0.73 <sup>h</sup>	7.2 <sup>h</sup>	–	10 <sup>i</sup>	–	3.1	–	–	[70]

<sup>a</sup>Specific surface area calculated by the BET method.

<sup>b</sup>Specific mesopore volume obtained by the NLDFT method.

<sup>c</sup>Quantities related to the final content of SiO<sub>2</sub> in the sample.

<sup>e</sup>Mesopore diameter calculated by the method in subscript.

<sup>f</sup>Lattice parameter of the pore lattice, calculated as a perfect lattice (PL) or real lattice (RL).

<sup>g</sup>Wall thickness calculated according to Equation (4): with the corresponding lattice parameter.

<sup>h</sup>Calculated through BJH.

<sup>i</sup>Calculated through small-angle XRD.

<sup>j</sup>Wall area calculated according to Equation (5) calculated from the perfect lattice data. TW refers to this work.

reduction in average diameter. This reduction is ca. 7% on average for the micropores, showing no clear trend with the NaBent content. This can be reasonably explained by proposing a mechanism where dissolved inorganics (such as Sodium silicate, formed from dissolving silica in the basic medium generated by NaBent) are deposited in the pore walls. It has been reported that processing in high pH solutions could be responsible for the changes in the pore dimension of SBA-15,<sup>[65]</sup> through the dissolution and reprecipitation of the silica in the pore walls. This trend is not maintained in the mesopores, possibly due to a protected environment due to the pores being filled with the Pluronic-P123 micelles. The data show an initial increase in the mesoporous radius, which is in agreement with the N<sub>2</sub> sorption analysis (Figure 8A,B).

Figure 11B shows a comparison between the mesoporous pore diameter results of the NLDFT and SAXS measurements. Both models show excellent agreement about the size of the pores in COK-12-600. On the contrary, a discrepancy of around 1 nm appears when comparing the portions corresponding to the NB-COK-X-M samples. Both observations can be explained by the increasing proportion of binders in the mixture and the fact that the NLDFT model's basis functions are obtained from pure silica materials. The average mesoporous diameter of the COK-12-600 grows initially ca. 34% when comparing the reference material and the binder-containing samples. Finally, a small change in the result of the pore diameter estimation can be observed between -M samples.

Figure 11C shows the cell parameter ( $a_0$ ) calculated from the (10) peak positions for the NB-COK-X-M samples.

Two results, which originate from considering a “perfect” hexagonal ordering or from allowing the spacing to be calculated as the average of a distribution of distances (“Real” lattice), are averaged and presented as a function of the NaBent content due to their agreement in terms of the overall trend and slight difference in value. The cell parameter changes considerably when the COK-12 is mixed with the NaBent, as mentioned previously, the maximum expansion of the lattice parameter with respect to that of COK-12-600 is ca. 11%. This can be explained by a swelling of the P123 micelles when exposed to a medium with high sodium concentration, like the one produced in the COK-12 and NaBent slurry.<sup>[69]</sup> The calculation also results in a slightly smaller lattice parameter for NB-COK-25-M (around 4% smaller), which seems in line with the previous observation of a smaller pore diameter.

Derived from the cell parameter and the pore diameter is the pore wall thickness, shown in Figure 11C. It can be observed that the lattice expansion does not compensate for the increase in pore diameter, leading to a thinner pore wall in NB-COK-X-M. Once again, NB-COK-25-M shows a small trend break, which differs from what would be expected from the literature.<sup>[70]</sup> The data produced in this study is insufficient to confirm whether this is a true break from the trend or could be attributed to other explanations, such as statistical or sample preparation errors.

Table 6 summarizes the measured and calculated quantities in this section and references a similar work, wherein OMS beads containing SBA-15 were produced, and the only thermal treatment was drying at 60°C. The lattice parameter and derived quantities were obtained from the

small angle portion of a regular XRD experiment.<sup>[70]</sup> Special attention must be paid to the column with the specific mesopore volume by silica weight. It can be clearly seen that while the pore volume is mainly conserved or slightly increases, no significant changes are observed for the reference SBA-15 material. In contrast, these experiments produced noticeable increases to the mesopores volume, as well as significantly larger pores, a reduction of the pore wall thickness and changes in the lattice parameter, which contrasts with the results reported by Cesario et al. where a maintained lattice parameter, smaller pore wall thickness and similar pore volume, with bigger pore diameters were found.

## 4 | CONCLUSIONS

Hierarchically porous silica monoliths were successfully robocasted, paving the way for developing an application-oriented slurry formulation for robocasting. The characteristics of the starting materials are mostly maintained, and the robocasting process allows for complex, well-defined geometries inaccessible by other means. The resulting monoliths have outstanding textural properties, especially in terms of internal mesopore volume. The impact of the increasing proportion of inorganic binder in the slurry, sodium bentonite (NaBent), was measured in the rheological properties of the generated pastes, as well as the pore structure and the mechanical strength of the printed and calcined monoliths.

In summary, uncalcined COK-12 and NaBent containing slurries with varying proportions (0, 13, 18 and 25%) of NaBent were successfully robocasted into stacked wood-pile shapes. The rheology of the slurries was modelled with the Herschel–Bulkley model. The flow index, yield stress, and consistency factor are altered with the content of NaBent (0.69 to 0.32, 96 vs. 259 Pa and 34–95 Pa  $s^{-n}$ ). The slurries analyzed are “printable” according to the Feilden printability and flow transition index printability criteria.

Furthermore, after sintering at 600°C, these monoliths showed geometrical porosity (49%–56%) close to the initial CAD (61%). This process also combined the template removal and the printed body’s sintering in one thermal treatment. The addition of NaBent affected the porous structure of the COK-12 in the monoliths, resulting in higher specific mesopore volume (0.52–0.67 g  $cm^{-3}$ ) than the bare COK-12 (0.48 g  $cm^{-3}$ ), a maintained hexagonal ordering of its pores, a larger cell parameter and pore diameter, and lower wall thickness when compared to calcined COK-12 powders while conserving the amorphous structure. The binder increased the compression strength

(0.2–1.0 MPa) and the apparent Young’s modulus (16–90 MPa) of the monoliths, while the monolith without binder could not withstand handling and measuring.

Future work might focus on using different binder systems or other soft-template materials to further increase pore volume, surface area, and mechanical strength. These results show potential in the applicability of COK-12-based monoliths for applications where pore volume and size are crucial factors, like gas adsorption and catalysis, but also where structured materials are preferable to powders such as environmental remediation, industrial chemical reactors and fossil-fueled vehicle exhausts.

## AUTHOR CONTRIBUTIONS

Emiliano S. Dal Molin: Conceptualization, methodology, formal analysis, investigation, data curation, writing—original draft, visualization, and project administration. Laura M. Henning: Conceptualization, investigation, methodology, writing—review & editing. Julian T. Müller: Investigation, writing—review & editing. Glen J. Smales: Conceptualization, methodology, software, validation, formal analysis, data curation, writing—review & editing, and visualization. Brian Pauw: Conceptualization, methodology, software, validation, formal analysis, data curation, writing—review & editing, and visualization. Maged F. Bekheet: Conceptualization, methodology, writing—review & editing, and supervision. Aleksander Gurlo: Conceptualization, resources, writing—review & editing, supervision, and funding acquisition. Ulla Simon: Conceptualization, methodology, writing—review & editing, and supervision.

## ACKNOWLEDGMENTS

The authors thank Daniel Werner from the Max Planck Institute of Colloids and Interfaces for the micro-CT measurements and Christina Eichenauer from TU Berlin for nitrogen sorption measurements. Emiliano Dal Molin thanks Onur Kaba, Mathias Czasny, for their help with robocasting and software set-up, Tatiana Mirson for her help with graphics and Benjamin Bischoff for his support and fruitful discussions during the writing of this manuscript. Emiliano Dal Molin was funded by the Einstein Foundation Berlin and UniSysCat.

Open access funding enabled and organized by Projekt DEAL.

## CONFLICT OF INTEREST STATEMENT

The authors declare no conflicts of interest.

## DATA AVAILABILITY STATEMENT

The data that support the findings of this study are available in the supplementary material of this article.


## ORCID

Emiliano S. Dal Molin  <https://orcid.org/0000-0002-1377-3999>

Julian T. Müller  <https://orcid.org/0000-0003-0703-8573>

Glen J. Smales  <https://orcid.org/0000-0002-8654-9867>

Maged F. Bekheet  <https://orcid.org/0000-0003-1778-0288>

Aleksander Gurlo  <https://orcid.org/0000-0001-7047-666X>

Ulla Simon  <https://orcid.org/0000-0001-6233-6595>

## REFERENCES

1. L. del-Mazo-Barbara, M.-P. Ginebra, *J. Eur. Ceram. Soc.* **2021**, *41*, 18.
2. E. Ordoñez, J. M. Gallego, H. A. Colorado, *Appl. Clay Sci.* **2019**, *182*, 105285.
3. S. Zhao, G. Siqueira, S. Drdova, D. Norris, C. Ubert, A. Bonnin, S. Galmarini, M. Ganobjak, Z. Pan, S. Brunner, G. Nyström, J. Wang, M. M. Koebel, W. J. Malfait, *Nature* **2020**, *584*, 387.
4. J. E. Smay, G. M. Gratson, R. F. Shepherd, J. Cesarano, J. A. Lewis, *Adv. Mater.* **2002**, *14*, 1279.
5. J. E. Smay, J. Cesarano, J. A. Lewis, *Langmuir* **2002**, *18*, 5429.
6. J. A. Lewis, *Adv. Funct. Mater.* **2006**, *16*, 2193.
7. E. Feilden, E. G.-T. Blanca, F. Giuliani, E. Saiz, L. Vandeperre, *J. Eur. Ceram. Soc.* **2016**, *36*, 2525.
8. L. Fiocco, H. Elsayed, D. Badocco, P. Pastore, D. Bellucci, V. Cannillo, R. Detsch, A. R. Boccaccini, E. Bernardo, *Biofabrication* **2017**, *9*, 25012.
9. L. Li, B. Li, M. Zhao, S. Ding, C. Zhou, *J. Biomed. Mater. Res. B Appl. Biomater.* **2011**, *98*, 230.
10. A. S. Diaz-Marta, S. Yañez, E. Lasorsa, P. Pacheco, C. R. Tubío, J. Rivas, Y. Piñeiro, M. A. G. Gómez, M. Amorín, F. Guitián, A. Coelho, *ChemCatChem* **2020**, *12*, 1762.
11. N. A. Sather, H. Sai, I. R. Sasselli, K. Sato, W. Ji, C. V. Synatschke, R. T. Zambrotta, J. F. Edelbrock, R. R. Kohlmeyer, J. O. Hardin, J. D. Berrigan, M. F. Durstock, P. Mirau, S. I. Stupp, *Small* **2021**, *17*, e2005743.
12. B. Jiang, Y. Yao, Z. Liang, J. Gao, G. Chen, Q. Xia, R. Mi, M. Jiao, X. Wang, L. Hu, *Small* **2020**, *16*, e1907212.
13. M. Zhang, W. Liu, Q. Lin, C. Ke, *Small* **2023**, <https://doi.org/10.1002/smll.202300323>.
14. M. J. Bessa, F. Brandão, M. Viana, J. F. Gomes, E. Monfort, F. R. Cassee, S. Fraga, J. P. Teixeira, *Environ. Res.* **2020**, *184*, 109297.
15. J. Lefevre, M. Gysen, S. Mullens, V. Meynen, J. van Noyen, *Catal. Today* **2013**, *216*, 18.
16. H. Thakkar, S. Eastman, A. Al-Mamoori, A. Hajari, A. A. Rownaghi, F. Rezaei, *ACS Appl. Mater. Interfaces* **2017**, *9*, 7489.
17. P. T. Smith, A. Basu, A. Saha, A. Nelson, *Polymer* **2018**, *152*, 42.
18. F. Magzoub, X. Li, S. Lawson, F. Rezaei, A. A. Rownaghi, *Fuel* **2020**, *280*, 118628.
19. T. Ludwig, J. Seckendorff, C. Troll, R. Fischer, M. Tonigold, B. Rieger, O. Hinrichsen, *Chem. Ing. Tech.* **2018**, *90*, 703.
20. E. Bogdan, P. Michorczyk, *Materials (Basel, Switzerland)* **2020**, *13*.
21. M. R. Hartings, Z. Ahmed, *Nat. Rev. Chem.* **2019**, *3*, 305.
22. C. Hurt, M. Brandt, S. S. Priya, T. Bhatelia, J. Patel, P. Selvakannan, S. Bhargava, *Catal. Sci. Technol.* **2017**, *7*, 3421.
23. C. Parra-Cabrera, C. Achille, S. Kuhn, R. Ameloot, *Chem. Soc. Rev.* **2018**, *47*, 209.
24. J. F. Le Page, J. Miquel, *In: Preparation of Catalysts I—Scientific Bases for the Preparation of Heterogeneous Catalysts, Proceedings of the First International Symposium held at the Solvay Research Centre, Vol. 1*, Elsevier **1976**, p. 39.
25. M. Dinkgreve, J. Paredes, M. M. Denn, D. Bonn, *J. Non-Newtonian Fluid Mech.* **2016**, *238*, 233.
26. E. Magnon, E. Cayeux, *Fluids* **2021**, *6*, 157.
27. P. C. F. Møller, J. Mewis, D. Bonn, *Eur. Phys. J. E Soft Matter* **2006**, *2*, 274.
28. Z. Chen, Z. Li, J. Li, C. Liu, C. Lao, Y. Fu, C. Liu, Y. Li, P. Wang, Y. He, *J. Eur. Ceram. Soc.* **2019**, *39*, 661.
29. L. F. Giraldo, B. L. López, L. Pérez, S. Urrego, L. Sierra, M. Mesa, *Macromol. Symp.* **2007**, *258*, 129.
30. C. M. A. Parlett, K. Wilson, A. F. Lee, *Chem. Soc. Rev.* **2013**, *42*, 3876.
31. T. Yokoi, *J. Jpn. Petrol. Inst.* **2012**, *55*, 13.
32. T. Asefa, Z. Tao, *Can. J. Chem.* **2012**, *90*, 1015.
33. A. Vinu, K. Z. Hossain, K. Ariga, *J. Nanosci. Nanotech.* **2005**, *5*, 347.
34. V. Meynen, P. Cool, E. F. Vansant, *Microporous Mesoporous Mater.* **2009**, *125*, 170.
35. F. Kleitz, S. H. Choi, R. Ryoo, *Chem. Commun. (Camb.)* **2003**.
36. A. A. Nada, M. F. Bekheet, S. Roualdes, A. Gurlo, A. Ayral, *J. Mol. Liq.* **2019**, *274*, 505.
37. J. Jammaer, A. Aerts, J. D'Haen, J. W. Seo, J. A. Martens, *J. Mater. Chem.* **2009**, *19*, 8290.
38. J. Jammaer, T. S. van Erp, A. Aerts, C. E. A. Kirschhock, J. A. Martens, *J. Am. Chem. Soc.* **2011**, *133*, 13737.
39. L. M. Henning, D. D. Cubas, M. G. Colmenares, J. Schmidt, M. F. Bekheet, B. R. Pauw, A. Gurlo, U. Simon, *Microporous Mesoporous Mater.* **2019**, *280*, 133.
40. L. M. Henning, U. Simon, A. Gurlo, G. J. Smales, M. F. Bekheet, *RSC Adv.* **2019**, *9*, 36271.
41. M. G. Colmenares, U. Simon, F. Schmidt, S. Dey, J. Schmidt, A. Thomas, A. Gurlo, *Microporous Mesoporous Mater.* **2018**, *267*, 142.
42. L. M. Henning, G. J. Smales, M. G. Colmenares, M. F. Bekheet, U. Simon, A. Gurlo, *Nano Select* **2023**, *4*, 202.
43. M. G. Colmenares, U. Simon, O. Cruz, A. Thomas, O. Goerke, A. Gurlo, *Microporous Mesoporous Mater.* **2018**, *256*, 102.
44. L. M. Henning, J. T. Müller, G. J. Smales, B. R. Pauw, J. Schmidt, M. F. Bekheet, A. Gurlo, U. Simon, *Nanoscale Adv.* **2022**, *4*, 3892.
45. M. G. Colmenares, U. Simon, M. Yildiz, S. Arndt, R. Schomaecker, A. Thomas, F. Rosowski, A. Gurlo, O. Goerke, *Catal. Commun.* **2016**, *85*, 75.
46. V. C. Ozalp, S. Ucak, A. D. Dursun, M. Sudagidan, O. Icin, C. Vakifahmetoglu, L. M. Henning, U. Simon, A. Gurlo, *J. Drug Delivery Sci. Technol.* **2023**, *86*, 104622.
47. S. Pulinthanathu Sree, E. Breynaert, C. E. A. Kirschhock, J. A. Martens, *Front Chem. Eng.* **2022**, *4*, 810443.
48. V. Dosarapu, S. Bandalla, M. Ravula, G. B. Bathula, S. Mavurapu, D. Shee, M. Varkolu, M. Baithy, C. S. Vasam, *Sustain. Energy Fuels* **2023**, *7*, 3609.
49. A. L. Khan, S. P. Sree, J. A. Martens, M. T. Raza, I. F. Vankelecom, *J. Membr. Sci.* **2015**, *495*, 471.
50. J. Schobing, M. Cesario, S. Dorge, H. Nouali, J. Patarin, J. Martens, J.-F. Brillhac, *Fuel Process. Technol.* **2021**, *211*, 106586.



51. M. Vialpando, A. Aerts, J. Persoons, J. Martens, G. van den Mooter, *J. Pharm. Sci.* **2011**, *100*, 3411.
52. G. Castruita-de León, Á. d. J. Montes-Luna, C. Y. Yeveirino-Miranda, G. Alvarado-Tenorio, H. I. Meléndez-Ortiz, O. Pérez-Camacho, L. A. García-Cerda, *Polym. Adv. Techs.* **2022**, *33*, 1412.
53. S. Lawson, X. Li, H. Thakkar, A. A. Rownaghi, F. Rezaei, *Chem. Rev.* **2021**, *121*, 6246.
54. H. Chen, A. Abdullayev, M. F. Bekheet, B. Schmidt, I. Regler, C. Pohl, C. Vakifahmetoglu, M. Czasny, P. H. Kamm, V. Meyer, A. Gurlo, U. Simon, *Fungal Biol. Biotechnol.* **2021**, *8*, 21.
55. G. J. Smales, B. R. Pauw, *J. Inst.* **2021**, *16*, P06034.
56. B. R. Pauw, A. J. Smith, T. Snow, N. J. Terrill, A. F. Thünemann, *J. Appl. Crystallogr.* **2017**, *50*, 1800.
57. J. Filik, A. W. Ashton, P. C. Y. Chang, P. A. Chater, S. J. Day, M. Drakopoulos, M. W. Gerring, M. L. Hart, O. V. Magdysyuk, S. Michalik, A. Smith, C. C. Tang, N. J. Terrill, M. T. Wharmby, H. Wilhelm, *J. Appl. Crystallogr.* **2017**, *50*, 959.
58. I. Breßler, J. Kohlbrecher, A. F. Thünemann, *J. Appl. Crystallogr.* **2015**, *48*, 1587.
59. ISO 17162:2014. *Fine ceramics (advanced ceramics, advanced technical ceramics): Mechanical properties of monolithic ceramics at room temperature — Determination of compressive strength.*
60. L. Bergström, *Colloids Surf. A* **1998**, *133*, 151.
61. A. Corker, H. C.-H. Ng, R. J. Poole, E. García-Tuñón, *Eur. Phys. J. E Soft Matter* **2019**, *15*, 1444.
62. L. A. Alcázar-Vara, J. Guerrero-Hernández, C. Chacon, I. R. Cortés-Monroy, *Energy sources, part A: recovery, utilization, and environmental effects.* **2021**, 1–14.
63. L. T. Zhuravlev, *Langmuir* **1987**, *3*, 316.
64. X. Li, Y. Xu, C. Li, *Acta Geotech.* **2020**, *15*, 1895.
65. G. Chandrasekar, M. Hartmann, V. Murugesan, *J. Porous Mater.* **2009**, *16*, 175.
66. M. Isabel Pariente, F. Martínez, J. Ángel Botas, J. Antonio Melero, *AIMS Environ. Sci.* **2015**, *2*, 154.
67. M. Thommes, K. Kaneko, A. V. Neimark, J. P. Olivier, F. Rodríguez-Reinoso, J. Rouquerol, K. S. Sing, *Pure Appl. Chem.* **2015**, *87*, 1051.
68. K. Holmberg, D. O. Shah, M. J. Schwuger (Eds.), *Handbook of applied surface and colloid chemistry*, Wiley, Chichester **2002**.
69. K. Deguchi, K. Meguro, *J. Colloid Interface Sci.* **1975**, *50*, 223.
70. M. Cesario, J. Schobing, F. Bruder, S. Dorge, H. Nouali, D. Habermacher, P. Kerdoncuff, M. Vierling, M. Moliere, J.-F. Brilhac, J. Patarin, *J. Porous Mater.* **2020**, *27*, 905.

## SUPPORTING INFORMATION

Additional supporting information can be found online in the Supporting Information section at the end of this article.

**How to cite this article:** E. S. Dal Molin, L. M. Henning, J. T. Müller, G. J. Smales, B. R. Pauw, M. F. Bekheet, A. Gurlo, U. Simon, *Nano Select.* **2023**, *1*. <https://doi.org/10.1002/nano.202300109>